

Article

Short-Time Impedance Spectroscopy Using a Mode-Switching Nonsinusoidal Oscillator: Applicability to Biological Tissues and Continuous Measurement

Tomiharu Yamaguchi ¹, Emiyu Ogawa ² and Akinori Ueno ^{1,*}

¹ Department of Electrical and Electronic Engineering, Tokyo Denki University, Tokyo 120-8551, Japan; 21769@ms.dendai.ac.jp

² School of Allied Health Science, Kitasato University, Kanagawa 252-0373, Japan; e.ogawa@kitasato-u.ac.jp

* Correspondence: ueno@mail.dendai.ac.jp; Tel.: +81-3-5284-5404

Abstract: Herein, we propose an impedance spectroscopy method using a mode-switching nonsinusoidal oscillator and apply this method for measuring the impedance of biological tissues and continuous impedance measurement. To obtain impedance spectra over a wide frequency range, we fabricated a novel nonsinusoidal oscillator incorporating binary counters and analog switches. This oscillator could periodically switch oscillation frequency through the mode switching of the feedback resistor. From the oscillation waveform at each oscillation frequency of this circuit (oscillator), we determined the impedance spectrum of a measured object using the discrete-time Fourier transform. Subsequently, we obtained the broad impedance spectrum of the measured object by merging odd-order harmonic spectral components up to the 19th order for each oscillation frequency. From the measured spectrum, the resistive and capacitive components of the circuit simulating bioimpedance were estimated with high accuracy. Moreover, the proposed method was used to measure the impedance of porcine myocardium; changes in the impedance spectrum of the myocardial tissue due to coagulation could be measured. Furthermore, rapid variations in the resistance value of a CdS photocell could be continuously measured using the proposed method.

Keywords: capacitive coupling; impedance spectroscopy; nonsinusoidal oscillator; DFT; frequency switching; biological application; continuous impedance measurement



Citation: Yamaguchi, T.; Ogawa, E.; Ueno, A. Short-Time Impedance Spectroscopy Using a Mode-Switching Nonsinusoidal Oscillator: Applicability to Biological Tissues and Continuous Measurement. *Sensors* **2021**, *21*, 6951. <https://doi.org/10.3390/s21216951>

Academic Editors: Maria Giovanna Trivella, Abdelhamid Errachid and Francesca G. Bellagambi

Received: 5 September 2021

Accepted: 18 October 2021

Published: 20 October 2021

Publisher's Note: MDPI stays neutral with regard to jurisdictional claims in published maps and institutional affiliations.



Copyright: © 2021 by the authors. Licensee MDPI, Basel, Switzerland. This article is an open access article distributed under the terms and conditions of the Creative Commons Attribution (CC BY) license (<https://creativecommons.org/licenses/by/4.0/>).

1. Introduction

Bioelectrical impedance analysis has become an important technique in the medical and healthcare fields [1–9]. Because the impedance of a living body (bioimpedance) depends on body composition, such as the water content of the body, it reflects medical conditions [10–13]. Thus, the absolute value and phase of bioimpedance are used to diagnose diseases, and this process is known as bioelectric impedance vector analysis [14–19]. Impedance measurement is also used in catheter ablation for treating arrhythmia [20–23]. By measuring the local impedance at an ablation site with electrodes integrated into an ablation catheter, the cauterization of myocardial tissue can be monitored. In the medical field, impedance may be measured using a single frequency or a few frequencies. However, bioimpedance has frequency characteristics over a wide range of frequencies, which originate from impedance components such as intracellular fluid resistance, extracellular fluid resistance, and the capacitance of cell membranes. Because cell membranes are highly insulating and cell fluids have ionic conductivity, in a low-frequency range, the current barely flows within cells but flows through the gaps among cells. Conversely, in a high-frequency range, the impedance caused by the capacitance of cell membranes decreases, meaning the current flows uniformly inside and outside cells. Therefore, if the impedance spectrum over a wide frequency range could be measured rapidly and conveniently, more detailed information about biological tissues could be obtained, which would be useful for diagnosing and treating medical conditions.

Impedance measurement generally involves coupling an electrode to a measured object through resistive coupling. Therefore, noninvasive impedance spectroscopy targeting insulated resistors, for instance, a living body covered with insulator-like clothing, has rarely been performed. To address this gap, we previously proposed capacitive coupling impedance spectroscopy (CIS) as a noninvasive technique for measuring impedance spectra through an insulation coating [24]. In this method, the measured object and capacitive coupling part are incorporated into an oscillation circuit. The oscillation frequency of the circuit depends on the coupling capacitance and the impedance of the measured object. Thus, even if the equivalent circuit model of the measured object is unknown, the change in these parameters can be monitored by measuring the oscillation frequency. This is applicable to monitoring a body movement and the breathing effort of a living body [25]. However, the equivalent circuit parameters of the measured object cannot be uniquely determined by only the oscillation frequency.

The frequency spectrum of the complex impedance of the measured object is obtained in a short time by analyzing the obtained oscillation waveform using the discrete-time Fourier transform (DFT), which allows estimating the resistance and capacitance components of the measured object. Therefore, CIS can be applied to not only measurement applications such as ablation by resistively contacting electrodes to biological tissue but also the measurement of biological impedance through an insulator such as clothing. Consequently, it is suitable for fabricating portable/wearable measurement systems. Furthermore, because the impedance spectrum is obtained from the oscillation waveform in every cycle, it enables an almost continuous impedance measurement. Continuous measurement of the impedance spectrum can be used to monitor biological processes such as cell differentiation [26].

In our previous CIS measurement, we used a nonsinusoidal oscillator incorporated into the measured object to estimate the impedance spectrum. DFT analysis of the nonsinusoidal wave obtained from this oscillator can determine the impedance at the fundamental frequency of the waveform and its odd harmonic frequencies. If the coupling capacitance is constant, and the measurement system has a high signal-to-noise ratio, the equivalent circuit parameters can be determined via less frequency points. However, in practical application, the coupling capacitance is often unknown and may fluctuate. To determine the equivalent circuit parameters of the measured object with high accuracy, we must estimate the impedance spectrum in the frequency range where the impedance has high frequency dependence. However, the oscillation frequency range of the nonsinusoidal oscillator is limited by the feedback resistance of it. Therefore, the feedback resistance cannot be set appropriately for an unknown coupling capacitance, and the impedance spectrum in the frequency range required for circuit parameter estimation may not be measured.

To solve this problem, we designed a nonsinusoidal oscillator that can change the oscillation frequency drastically by switching several feedback resistors. Using the significantly different values of the feedback resistances, even if the coupling capacitance fluctuates, one of the feedback resistors can cover the frequency range required for circuit parameter estimation and thus leads to a stable and high estimation accuracy.

Furthermore, high electrical noise may reduce the measurement accuracy of the impedance spectrum. In this measurement environment, it is difficult to estimate the circuit parameters accurately with less frequency points. Our proposed frequency-switchable (mode-switching) oscillator enables impedance measurement with many frequency points by merging the frequency spectra for each feedback resistance.

To apply our proposed nonsinusoidal oscillator to bioimpedance measurement, this study aimed to demonstrate the following four outcomes using CIS:

- (1) Design a nonsinusoidal oscillation circuit capable of periodically switching oscillation frequency;
- (2) Show that the proposed method can estimate circuit parameters for circuit models close to actual measured objects;
- (3) Apply the proposed method to the impedance measurement of biological tissues;

- (4) Show that the continuous measurement of impedance is possible.

2. Capacitive Coupling Impedance Spectroscopy

2.1. Mode-Switching Nonsinusoidal Oscillator

In CIS, a nonsinusoidal oscillator circuit, such as a Schmitt trigger inverter oscillator, is used. Although this oscillation circuit does not have a high-accuracy oscillation frequency, it allows constructing a system that is small, inexpensive, and easy to handle because it has few parts, and the oscillation is stable. In our previous CIS study, the impedance of the measured object at the fundamental frequency (oscillation frequency) and odd-order harmonics were determined using DFT analysis of the oscillation waveforms. However, in some cases, the impedance spectra of sufficient data points cannot be obtained with a single oscillation frequency, and the estimation accuracy decreases when the circuit parameters are estimated using an equivalent circuit model. To address this problem, we designed a novel mode-switching nonsinusoidal oscillator that can switch among multiple oscillating frequencies.

Figure 1 shows a schematic of the mode-switching nonsinusoidal oscillator. A nonsinusoidal oscillation waveform corresponding to the impedance of the measured object is obtained by incorporating the measured object, capacitively coupled with the electrode, into the oscillation circuit. \dot{Z}_X represents the impedance of the measured object, including capacitive coupling, whose circuit parameters differ depending on the equivalent circuit model of the measured object. For example, in the case of bioimpedance, it comprises extracellular fluid resistance R_X , intracellular fluid resistance R_{PX} , and the capacitance of cell membranes C_{PX} [27,28]. In particular, $R_{PX} = 0 \Omega$ for skin impedance [29]. \dot{Z}_{X1} is the impedance of the measured object excluding capacitive coupling. Capacitances C_{SX1} and C_{SX2} correspond to the coupling capacitance between the insulator and electrode. \dot{Z}_A is the combined impedance of resistance R_A and parasitic capacitance C_A . The current $i_{12}(t)$ flowing into \dot{Z}_X is calculated from the voltage $v_1(t)$ generated in \dot{Z}_A (I/V conversion). The resistance R_A represents the resistance for measuring the current. C_A represents a parasitic component caused by the parasitic capacitance of the circuit board, input capacitance of the probe of the oscilloscope, and other factors. The feedback resistance R_F of the oscillator circuit comprises resistors R_{F1} , R_{F2} , and R_{F3} connected in series. The Schmitt trigger inverter switches the high and low levels of the voltage $v_{OSC}(t)$, V_H and V_L , by the input voltage $v_2(t)$. The voltage $v_2(t)$ changes by the charge/discharge of the capacitors connected on the input side of the Schmitt trigger inverter, which causes the square wave of the voltage $v_{OSC}(t)$. In addition, square-like and triangle-like waveforms are generated as $v_1(t)$ and $v_2(t)$, respectively. Because the charging/discharging speed of the capacitors is determined by the current $i_{12}(t)$ flowing through \dot{Z}_X , the oscillation frequency depends on \dot{Z}_X , \dot{Z}_A , and R_F . If \dot{Z}_X is a resistive element R_X and capacitive coupling C_{SX} in series, and parasitic capacitance C_A can be ignored, the oscillation frequency f_0 can be expressed with the following [24]:

$$f_0 = \frac{1}{(R_F + R_A + R_X)C_{SX} \left(\ln \frac{V_H - V_A}{V_H - V_P} + \ln \frac{V_B - V_L}{V_N - V_L} \right)}, \quad (1)$$

$$V_A = V_N + \frac{R_A + R_X}{R_F + R_A + R_X} (V_H - V_L), \quad (2)$$

$$V_B = V_P - \frac{R_A + R_X}{R_F + R_A + R_X} (V_H - V_L), \quad (3)$$

where $C_{SX} = C_{SX1}C_{SX2}/(C_{SX1} + C_{SX2})$ denotes the combined capacitance of C_{SX1} and C_{SX2} . V_P and V_N are the threshold voltages of the Schmitt trigger inverter. If \dot{Z}_X has a more complex circuit network, these equations are not strictly valid, but the oscillation frequency can be roughly estimated using these equations.

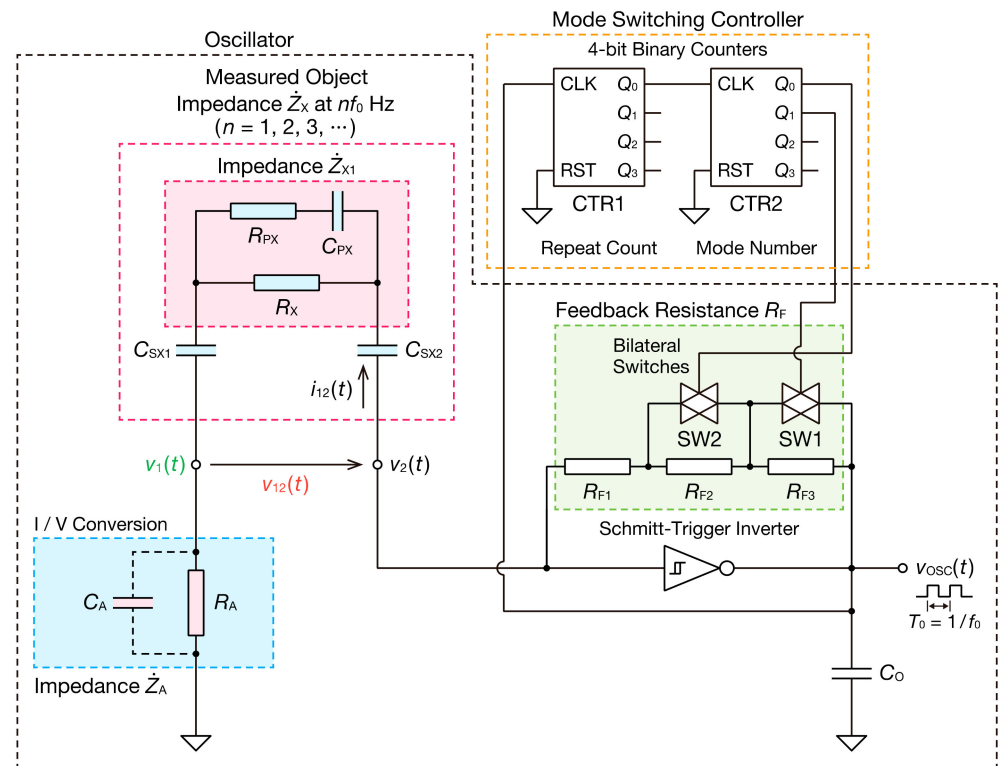


Figure 1. Mode-switching nonsinusoidal oscillator. The oscillation frequency f_0 and the oscillation period T_0 of the oscillator are switched between four different frequencies by 4-bit binary counters and bilateral analog switches. CLK of 4-bit binary counters denotes a clock signal, and RST represents a reset signal. Q_0 , Q_1 , Q_2 , and Q_3 of 4-bit binary counters denote zero bits, and the first, second, and third bits of the output signals, respectively. C_o represents a bypass capacitor to remove the switching noise in the oscillator, and its value is 0.47 nF. CTR1 and CTR2 are binary counters to control the repeat count and the mode number of the mode switching, respectively.

Because the operation of the bilateral switches can cause an unstable oscillation such as switching noise, we used the 4-bit binary counter CTR1 to stabilize the oscillation. The counter CTR1 controls the repeat count for switching the feedback resistors. The square wave signal $v_{osc}(t)$ of the oscillator is input to the counter CTR1 as the clock signal. The 0-bit output Q_0 of the counter CTR1 has half the frequency of $v_{osc}(t)$. For this reason, the bilateral switches operate every two cycles of the oscillation waveform for each R_F , and the oscillation of the second half cycle becomes stable.

Subsequently, the frequency-divided square wave signal is input as a clock signal to the counter CTR2. CTR2 determines the mode number obtained from the mode switching of the oscillator. Moreover, the 0-bit and 1-bit outputs Q_0 and Q_1 of the counter CTR2 are input as the control signals of the bilateral switches SW1 and SW2, respectively. Because R_{F2} or R_{F3} is short circuited when the switch is ON, R_F is switched every two cycles of the oscillation waveform in four modes: R_{F1} , $R_{F1} + R_{F2}$, $R_{F1} + R_{F3}$, and $R_{F1} + R_{F2} + R_{F3}$ (Table 1). Therefore, the oscillation frequency can be switched periodically.

Table 1. Four different modes of the feedback resistance R_F .

Mode	Q_1	Q_0	SW1	SW2	R_F
1	0	0	OFF	OFF	$R_{F1} + R_{F2} + R_{F3}$
2	0	1	OFF	ON	$R_{F1} + R_{F3}$
3	1	0	ON	OFF	$R_{F1} + R_{F2}$
4	1	1	ON	ON	R_{F1}

0 and 1 indicate a low level and a high level of a square wave, respectively.

The procedure for estimating impedance is determined using a previously reported procedure [24]. The voltages $v_1(t)$ and $v_{12}(t)$ measured in the circuit, shown in Figure 1, form the periodic nonsinusoidal waveforms of the oscillation frequency f_0 . Therefore, the Fourier series expansion of the one cycle of the observed waveform comprises a sine wave of the fundamental frequency f_0 and its integer multiple kf_0 ($k = 1, 2, 3, \dots$), and the coefficients of each frequency component are obtained as the amplitude and phase spectra through the DFT of the section concerned. From the obtained amplitude and phase spectra, \dot{Z}_X can be calculated using the following equation:

$$\dot{Z}_X(kf_0) = \frac{\dot{V}_{12}(kf_0)}{\dot{I}_{12}(kf_0)} = \frac{|\dot{V}_{12}(kf_0)|}{|\dot{V}_1(kf_0)|} \cdot |\dot{Z}_A(kf_0)| e^{j\{\theta_{V12}(kf_0) - \theta_{V1}(kf_0) + \theta_{ZA}(kf_0)\}}, \quad (4)$$

where $\dot{V}_{12}(kf_0)$ and $\dot{V}_1(kf_0)$ denote the complex voltages of $v_{12}(t)$ and $v_1(t)$, respectively; $\dot{I}_{12}(kf_0)$ denotes the complex current of $i_{12}(t)$; $|\dot{V}_{12}(kf_0)|$ and $\theta_{V12}(kf_0)$ represent the amplitude and phase of the complex voltage at \dot{Z}_X ; $|\dot{V}_1(kf_0)|$ and $\theta_{V1}(kf_0)$ represent the amplitude and phase of the complex voltage at \dot{Z}_A ; and $|\dot{Z}_A(kf_0)|$ and $\theta_{ZA}(kf_0)$ represent the magnitude and phase of the impedance \dot{Z}_A , respectively. The impedance estimation using Equation (4) is valid for any periodic waveform of $v_{12}(t)$ and $v_1(t)$ because Equation (4) is applied to each frequency component obtained from the oscillation waveform of $v_{12}(t)$ and $v_1(t)$. The real and imaginary parts of the impedance \dot{Z}_X , $\text{Re}(\dot{Z}_X)$ and $\text{Im}(\dot{Z}_X)$, are obtained with Equations (5) and (6):

$$\text{Re}(\dot{Z}_X) = \frac{|\dot{V}_{12}(nf_0)|}{|\dot{V}_1(nf_0)|} \cdot |\dot{Z}_A(nf_0)| \cos\{\theta_{V12}(nf_0) - \theta_{V1}(nf_0) + \theta_{ZA}(nf_0)\}, \quad (5)$$

$$\text{Im}(\dot{Z}_X) = \frac{|\dot{V}_{12}(nf_0)|}{|\dot{V}_1(nf_0)|} \cdot |\dot{Z}_A(nf_0)| \sin\{\theta_{V12}(nf_0) - \theta_{V1}(nf_0) + \theta_{ZA}(nf_0)\}. \quad (6)$$

We can obtain the oscillation waveform with multiple oscillation frequencies using the mode-switching oscillator. Therefore, one synthesized impedance spectrum is obtained by merging the spectral data for each oscillation frequency.

If it is known that \dot{Z}_X is a series connection of the resistor R_X and the capacitive coupling C_{SX} , R_X and C_{SX} can be estimated using the least squares method for a finite number of frequency spectra nf_0 ($n = 1, 2, 3, \dots, N$).

$$\text{Re}(\dot{Z}_X) = R_X, \quad (7)$$

$$\text{Im}(\dot{Z}_X) = -\frac{1}{2\pi n f_0 C_{SX}}. \quad (8)$$

Furthermore, when \dot{Z}_X is the common bioimpedance (Figure 1) equivalent circuit model,

$$\text{Re}(\dot{Z}_X) = \frac{(2\pi n f_0 C_{PX})^2 (R_X R_{PX}^2 + R_X^2 R_{PX}) + R_X}{(2\pi n f_0 C_{PX})^2 (R_{PX} + R_X)^2 + 1}, \quad (9)$$

$$\text{Im}(\dot{Z}_X) = -\frac{1}{2\pi n f_0 C_{SX}} - \frac{2\pi n f_0 C_{PX} R_X^2}{(2\pi n f_0 C_{PX})^2 (R_{PX} + R_X)^2 + 1}. \quad (10)$$

Similarly, the circuit parameters can be estimated using the least squares method. When $R_{PX} = 0 \Omega$, Equations (9) and (10) represent the real and imaginary parts of the

circuit comprising the parallel-connected R_X and C_{PX} (RC parallel circuit) and coupling capacitance C_{SX} , respectively.

2.2. Experimental Method

2.2.1. CIS of Parallel RC Circuits and Bioimpedance Models

A readily available 74HC14AP (Toshiba, Japan) was used as the Schmitt trigger inverter integrated circuit (IC), as illustrated in Figure 1. The typical V_P and V_N values of 74HC14AP in Equations (1)–(3) are 3.5 V and 2.3 V at 6 V of the supply voltage, respectively. A TC4520BP (Toshiba, Japan) was used as the 4-bit binary counter IC, and a TC74HC4066AP (Toshiba, Japan) was used as the bilateral analog switch IC. The power supply voltage of these ICs was set to 6 V, and V_H and V_L were set to 6 V and 0 V, respectively. Z_A was considered to consist only of the resistor R_A . R_A was set to 0.20 Ω . There is typically C_A of several tens of pF due to the parasitic components such as the probe capacity of the oscilloscope, but C_A is negligible because R_A is sufficiently small. The oscillator was designed to measure the impedance of biological tissue with a resistance of less than 1 k Ω and a capacitance of several nF. We selected four fundamental frequencies so that they contribute to an accurate estimation of the measured impedance parameters based on preliminary experiments. Two sets of the fundamental frequencies obtained by combining R_{F1} , R_{F2} , and R_{F3} are shown in Table 2.

Table 2. Two sets of the oscillation frequencies obtained by combining R_{F1} , R_{F2} , and R_{F3} .

Set	R_{F1} (k Ω)	R_{F2} (k Ω)	R_{F3} (k Ω)	4 Modes of R_F (k Ω)	Estimated Oscillation Frequencies (kHz)
1	3.3	1.8	3	8.1, 6.3, 5.1, 3.3	16.9, 22.3, 28.4, 47.9
2	5.1	1	2	8.1, 7.1, 6.1, 5.1	16.9, 19.5, 23.1, 28.4

The oscillation frequencies were estimated using Equations (1)–(3) with $R_X = 0 \Omega$. The actual oscillation frequencies depend on Z_X .

First, circuit parameters comprising the RC parallel circuit (R_X and C_{PX}) and coupling capacitance C_{SX} were estimated using CIS. Metal film resistors and polypropylene (PP) film capacitors with known resistance and capacitance values were incorporated into the circuit as resistance R_X and capacitance C_{PX} , C_{SX} . To demonstrate that our proposed method can estimate C_{PX} with various values, we set the capacitance of 1.016 or 9.85 nF as C_{PX} . The coupling capacitance C_{SX} was set to 9.76 nF. We used the combination of set 1 in Table 2 as R_{F1} , R_{F2} , and R_{F3} . These feedback resistors enable determining the impedance spectrum in a wider frequency range.

Further, we estimated the circuit parameters of the bioimpedance model (R_X , R_{PX} , C_{PX} , and C_{SX}) with the coupling capacitance using CIS. The estimation of R_{PX} is more difficult than that of R_X because it is affected by the accuracy of the impedance estimated using higher-order harmonics. For this reason, we evaluated the estimation accuracy of R_{PX} in more detail. Resistance with a constant value of 0.30 k Ω was used as R_X . C_{PX} was set to 3.22 nF, which simulates the capacitance with biological tissue. C_{SX} was set to 9.76 nF. To obtain many frequency points at lower frequencies, we used the combination of set 2 in Table 2 as R_{F1} , R_{F2} , and R_{F3} .

In these experiments, we prepared ten resistors as R_X or R_{PX} with different resistances from 0.10 to 1.0 k Ω and set the coupling capacitance C_{SX} to 9.76 nF.

2.2.2. Application of CIS to Biological Tissues

To demonstrate that the impedance spectrum of biological tissues can be measured using this CIS system, we measured the impedance of porcine myocardium. The coagulation of the myocardium causes tissue degeneration and decreases the impedance of the coagulated part [30]. Therefore, porcine myocardium samples were coagulated through electrocautery to determine whether the change in impedance before and after the coagulation could be measured. Three porcine hearts were prepared, and the myocardium

of each left ventricle was ablated in four locations (Figure 2a). Counter electrodes were placed across the back of the porcine myocardium, and it was coagulated through electrocautery for 30 s at a power of 30 W. The electrocautery was set to the soft coagulation mode. Moreover, measuring electrodes were set up, as illustrated in Figure 2b, with circular electrodes on either side of the ablation point. The electrodes were spaced 10 mm apart and directly contacted at the same position of the myocardium before and after each coagulation. The impedance generated when the electrode and myocardial tissue come into contact forms a resistive coupling. Therefore, the coupling capacitance is extremely small, meaning the oscillating frequency of the mode-switching nonsinusoidal oscillator increases. A PP film capacitor of $C_{SX} = 9.76$ nF was connected in series between the electrode and oscillation circuit so that the oscillation frequency was reduced to approximately 20 kHz. R_{F1} , R_{F2} , and R_{F3} were 3.3, 1.8, and 3.0 k Ω (set 1), respectively.

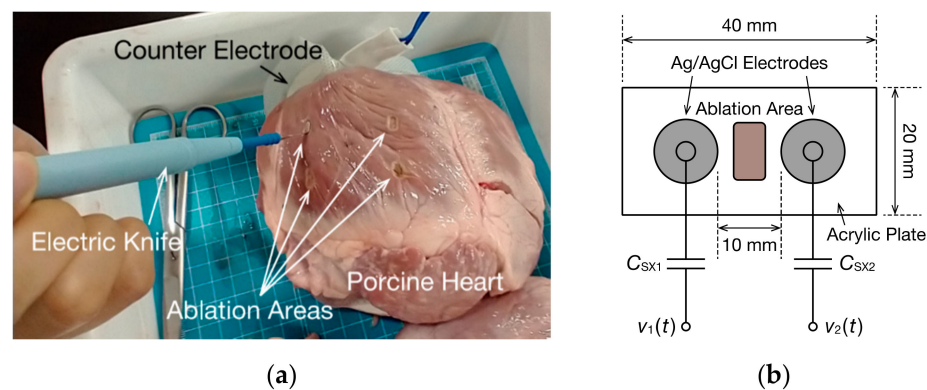


Figure 2. Impedance measurement of porcine myocardium: (a) photograph of the porcine left ventricle coagulated using electrocautery; (b) measurement electrode fixture.

2.2.3. Continuous Impedance Measurement Using CIS

Furthermore, a CdS photocoupler (LCR0203, Nanyang Senba Optical and Electronic, Shenzhen, China) was incorporated into the oscillator circuit as a part of \tilde{Z}_X , and the temporal change in R_X and R_{PX} could be measured using the proposed method. CdS photocells can be regarded as simple resistors. Moreover, increasing the current I_{Ph} flowing through a light-emitting diode (LED) built in the CdS photocoupler decreases the resistance value of the CdS photocell. Therefore, the resistance value can be changed over time by changing the current I_{Ph} of the LED. This current was controlled via a constant current circuit using an operational amplifier (NJU7032D, NJR, Tokyo, Japan) and an N-channel field-effect transistor (2N7000, ON Semiconductor, Phoenix, USA), as illustrated in Figure 3. In this circuit, the current I_{Ph} can be controlled in the range 0.6–10 mA by adjusting the voltage V_C between 0.12 and 2 V. The capacitive coupling C_{SX} was set to 9.76 nF. First, it was measured when only the photocell was connected as a resistor R_X via C_{SX} (Figure 3a). In this case, the counter IC and analog switch IC of the mode-switching nonsinusoidal oscillator were not used because the parameters could be estimated sufficiently accurately with a single mode of R_F . Only the R_{F1} of 8.2 k Ω was connected as R_F . Subsequently, the temporal change in the impedance spectrum was determined from the oscillation waveform of the oscillator using the bioimpedance model and C_{SX} (Figure 3b,c). R_{F3} is short circuited so that the oscillation frequency is switched in two modes to increase the temporal resolution. R_{F1} and R_{F2} were 3.3 and 1.8 k Ω , respectively.

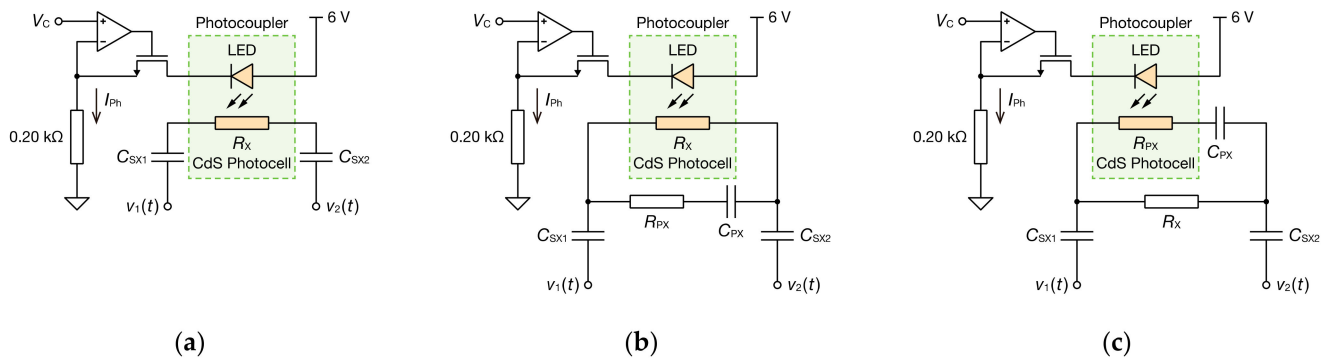


Figure 3. Constant current circuit for the LED current control of the photocoupler. The CdS photocell was used as (a) a single resistor, (b) a resistor R_X of the bioimpedance model, or (c) R_{PX} of its model.

2.2.4. Data Acquisition and DFT Analysis

Time waveform data of voltages were collected using a digital oscilloscope (PicoScope 5444D, Pico Technology, Cambridgeshire, UK). $v_1(t)$ and $v_2(t)$ in Figure 1 were measured, and time waveform data for $v_{12}(t)$ were obtained from the difference between them. Thereafter, DFT was performed for the obtained waveform data. When using the mode-switching function, the oscillation frequency is switched in four or two modes every two cycles. DFT was performed individually for the waveform of the second half cycle of each oscillation frequency, and the merged spectral data for the set of oscillation frequencies (one segment) were obtained. DFT was performed for every cycle of the oscillation waveform when mode switching was not used. A rectangular window was used for the window function of DFT. Furthermore, the impedance spectra for 10 segments were averaged, except for experiments using a CdS photocoupler. The real and imaginary parts of \vec{Z}_X were calculated from the obtained DFT data, and R_X , R_{PX} , C_{PX} , and C_{SX} were estimated via the least squares method using Equations (7) and (8) or (9) and (10). In the estimation using Equations (9) and (10), first, R_X , R_{PX} , and C_{PX} were estimated using Equation (9) from the DFT data of the real part of \vec{Z}_X . The estimated R_X , R_{PX} , and C_{PX} were then substituted into Equation (10), and C_{SX} was estimated from the DFT data of the imaginary part of \vec{Z}_X . In the circuit parameter estimation, odd-order harmonic components up to the 19th order obtained through DFT are used. However, because the frequency characteristics of the PP film capacitor and parasitic capacitance of the circuit board affect the estimation result in high-frequency ranges, harmonic components greater than 500 kHz when C_{PX} was less than 2.0 nF and harmonic components greater than 350 kHz when C_{PX} was 2.0 nF or higher were not used for estimation.

3. Results and Discussion

3.1. CIS of Parallel RC Circuits and Bioimpedance Models

Figure 4 illustrates oscillation waveforms when $R_X = 0.10$ k Ω , $R_{PX} = 0$ Ω , $C_{PX} = 1.016$ nF, and $C_{SX} = 9.76$ nF are connected as \vec{Z}_X in the mode-switching nonsinusoidal oscillator. R_F switched every two cycles, and the oscillation frequency changed in four modes. Oscillating frequencies when R_F was 8.1, 6.3, 5.1, and 3.3 k Ω were 14.0, 18.2, 23.2, and 38.4 kHz, respectively. The smaller values than the values estimated using Equation (1) may be because the actual threshold voltages of the Schmitt trigger IC are different from the typical values in the datasheet specification. The spike noise observed at 0.4 ms is due to the switching noise of the Schmitt trigger inverter. However, the spike noise has no effect on the estimation of the impedance spectrum because we used only the waveform of the second half cycle for DFT.

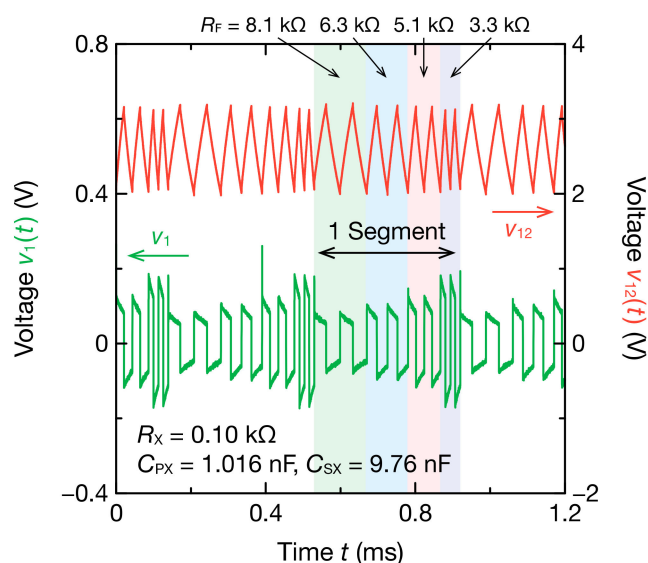


Figure 4. Four-mode oscillation waveforms of $v_1(t)$ and $v_{12}(t)$ obtained through the mode-switching nonsinusoidal oscillator. R_X , R_{PX} , C_{PX} , and C_{SX} were set to 0.10 k, 0 Ω , 1.016 nF, and 9.76 nF, respectively. The oscillation frequency was switched every two cycles of each R_F . The DFT analysis was performed on the oscillation waveforms of the second half of two cycles.

Figure 5 shows the spectra of \dot{Z}_X calculated using DFT analysis. By applying DFT to the oscillation waveform for each R_F , four modes of frequency spectra were obtained. These spectra agreed well with the theoretical values calculated from Equations (9) and (10) with $R_{PX} = 0 \Omega$. Even when the resistance and capacitance were large, such as $R_X = 0.91 \text{ k}\Omega$ and $C_{PX} = 9.85 \text{ nF}$, impedance spectra agreed well with the theoretical values (Figure 6).

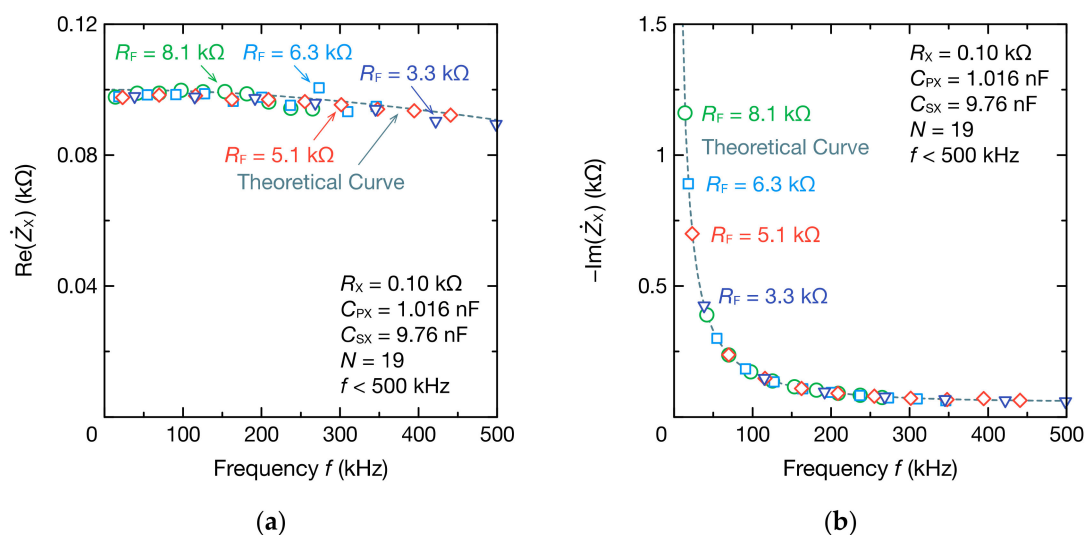


Figure 5. Frequency spectra of the (a) real part $\text{Re}(\dot{Z}_X)$ and (b) imaginary part $\text{Im}(\dot{Z}_X)$ of the impedance \dot{Z}_X comprising the resistance R_X of 0.10 k Ω , resistance R_{PX} of 0 Ω , capacitance C_{PX} of 1.016 nF (parallel RC circuit), and capacitance C_{SX} of 9.76 nF. The dashed lines represent the theoretical curves calculated from Equations (9) and (10).

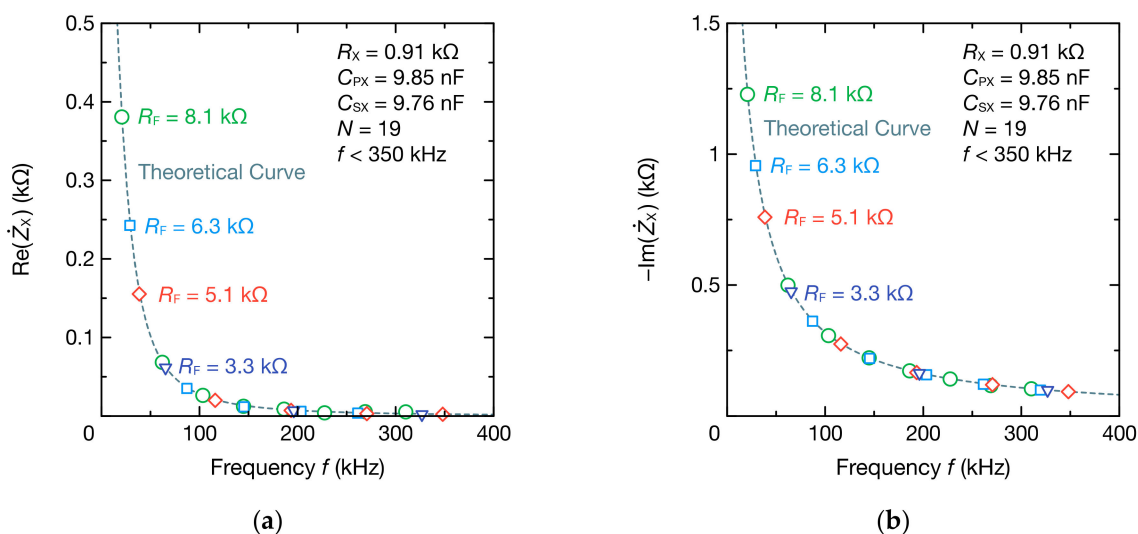


Figure 6. Frequency spectra of the (a) real part $\text{Re}(\dot{Z}_X)$ and (b) imaginary part $\text{Im}(\dot{Z}_X)$ of the impedance \dot{Z}_X comprising the resistance R_X of 0.91 k Ω , resistance R_{PX} of 0 Ω , capacitance C_{PX} of 9.85 nF (parallel RC circuit), and capacitance C_{SX} of 9.76 nF. The dashed lines represent the theoretical curves calculated from Equations (9) and (10).

Further, the values of R_X , C_{PX} , and C_{SX} were estimated from the impedance spectrum. Figure 7 illustrates the estimation values of R_X , C_{PX} , and C_{SX} . To verify the usefulness of the mode-switching function, the estimation was performed using the spectrum obtained from the four combinations of R_F and the spectrum obtained from one mode and two modes of R_F . The estimation error sometimes exceeded 2% when only DFT data obtained from one mode of R_F were used; however, the estimation accuracy improved when two modes of R_F were used. Moreover, each circuit parameter could be estimated with high accuracy, regardless of the value of R_X and C_{PX} , using the four modes of R_F . This demonstrates that the superposition of the impedance spectra through the mode-switching function improves the estimation accuracy of the circuit parameters.

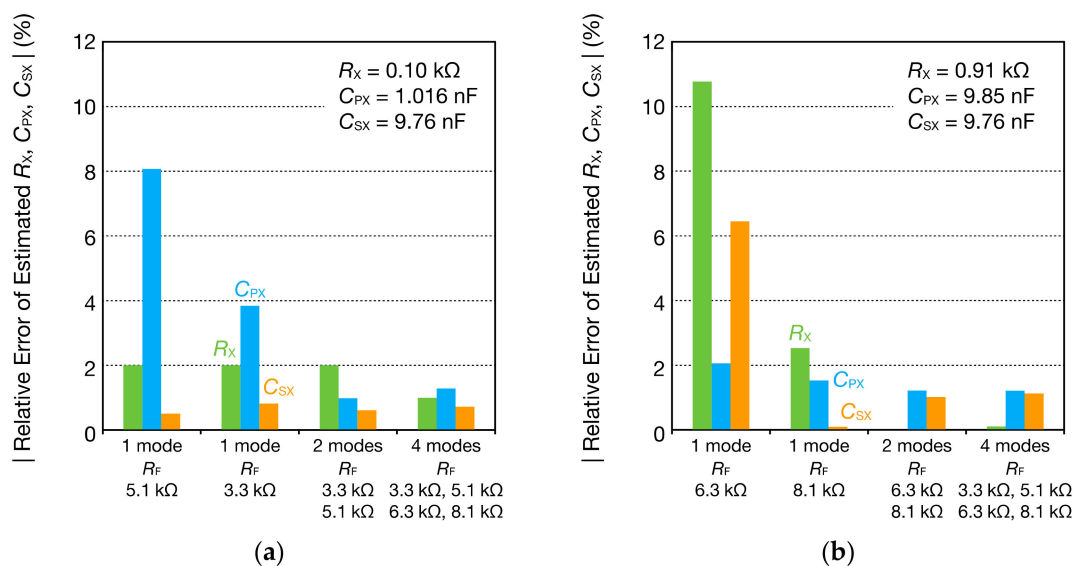


Figure 7. Absolute relative estimation errors of the circuit parameters of parallel RC circuits: (a) $R_X = 0.10$ k Ω , $C_{PX} = 1.016$ nF, and $C_{SX} = 9.76$ nF; (b) $R_X = 0.91$ k Ω , $C_{PX} = 9.85$ nF, and $C_{SX} = 9.76$ nF.

Subsequently, with $C_{PX} = 1.016$ nF and $C_{SX} = 9.76$ nF, we measured the impedance spectrum by changing R_X from 0.1 to 1 k Ω . Figure 8 shows some of the impedance spectra

obtained. The impedance spectra according to the values of R_X were obtained, and the fitting curves obtained from Equations (9) and (10) using the least squares method agreed well with the DFT data.

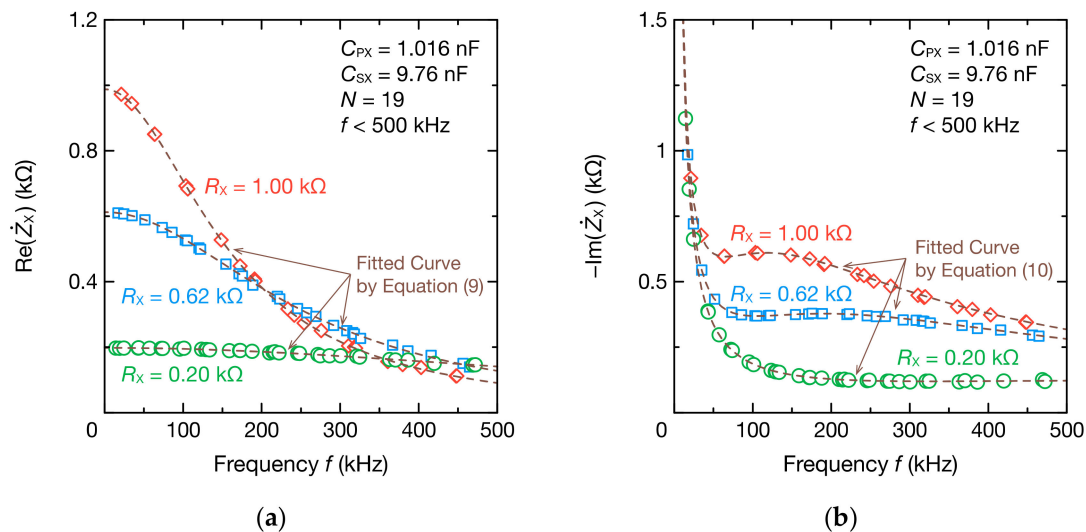


Figure 8. Frequency spectra of the (a) real part $\text{Re}(\dot{Z}_X)$ and (b) imaginary part $\text{Im}(\dot{Z}_X)$ of the impedance \dot{Z}_X comprising the parallel RC circuits for $C_{PX} = 1.016$ nF and coupling capacitance $C_{SX} = 9.76$ nF. The DFT data were fitted to Equations (9) and (10) to calculate R_X , C_{PX} , and C_{SX} (dashed lines).

When the circuit parameters were estimated, the estimation error of R_X was within 12Ω , and R_X could be accurately estimated from 0.1 to 1 k Ω (Figure 9a). Furthermore, the errors of C_{PX} and C_{SX} were within 1.28% and 0.82%, respectively, which are sufficiently small errors (Figure 9b,c). These results indicate that the circuit parameters of the RC parallel circuit can be estimated with high accuracy through capacitive coupling.

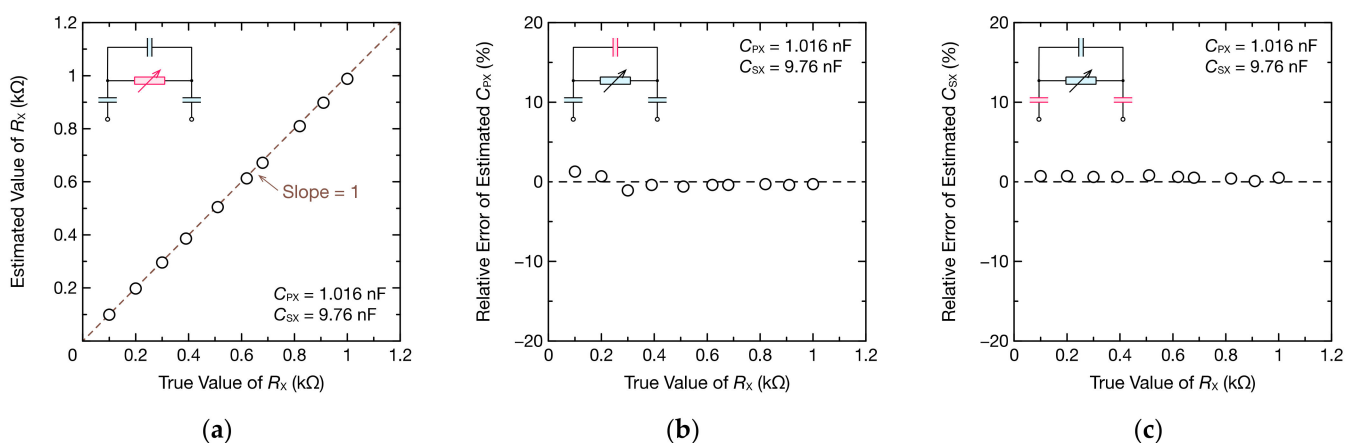


Figure 9. R_X , C_{PX} , and C_{SX} of the parallel RC circuits estimated using oscillation waveforms and DFT: (a) the estimated R_X , (b) relative error of the estimated C_{PX} , and (c) relative error of the estimated C_{SX} . The insets are the circuit model used for fitting, and the estimated parameters are highlighted in pink.

The impedance characteristics of a measured object are frequently discussed using Cole–Cole plots. The proposed method can obtain a wide frequency range spectrum using multiple values of R_F , and the Cole–Cole plots, as illustrated in Figure 10, can be easily obtained. The Cole–Cole plot of the impedance \dot{Z}_{X1} excluding capacitive coupling showed semicircles, and the radius of the semicircle increased with resistance R_X .

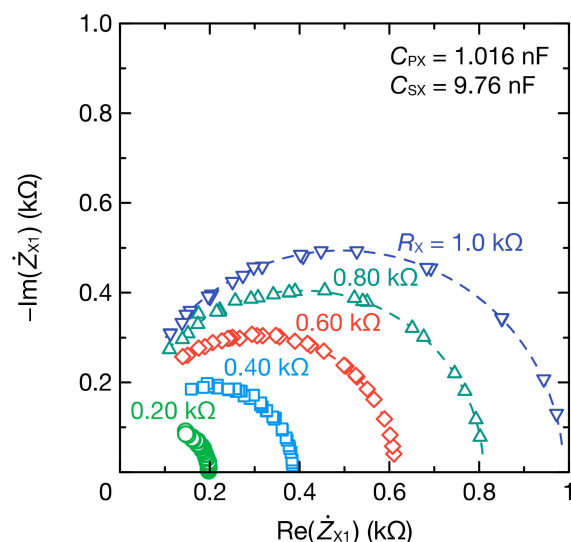


Figure 10. Cole–Cole plot of \dot{Z}_{X1} for the parallel RC circuits with $C_{PX} = 1.016$ nF and $C_{SX} = 9.76$ nF. The dashed lines represent the fitting curves obtained from Equations (9) and (10).

Moreover, we investigated whether the circuit parameters of the bioimpedance model could be estimated. Figure 11 shows the impedance spectrum of the bioimpedance model when R_{PX} was 0.20, 0.62, or 1.0 k Ω . Despite the small change in the real part compared with the RC parallel circuit due to the existence of R_{PX} , the fitting results using Equation (9) agreed well with the DFT data. The imaginary part could also be fitted accurately using Equation (10). Figure 12 shows the estimation results of R_X , R_{PX} , C_{PX} , and C_{SX} . The estimation errors of R_X and R_{PX} were within 6 and 11 Ω , respectively, which are sufficiently small estimation errors. The estimation errors of C_{PX} and C_{SX} were also within 3.79% and 1.03%, respectively.

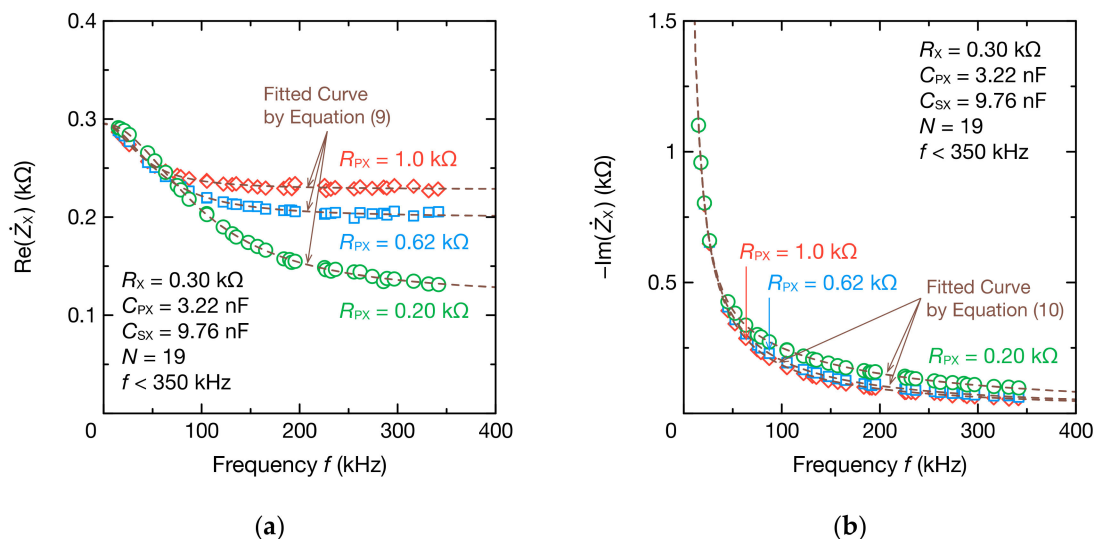


Figure 11. Frequency spectra of the (a) real part $\text{Re}(\dot{Z}_X)$ and (b) imaginary part $-\text{Im}(\dot{Z}_X)$ of the impedance \dot{Z}_X comprising the bioimpedance models for $R_X = 0.30$ k Ω , $C_{PX} = 3.22$ nF, and coupling capacitance $C_{SX} = 9.76$ nF. DFT data were fitted to Equations (9) and (10) to determine R_X , R_{PX} , C_{PX} , and C_{SX} (dashed lines).

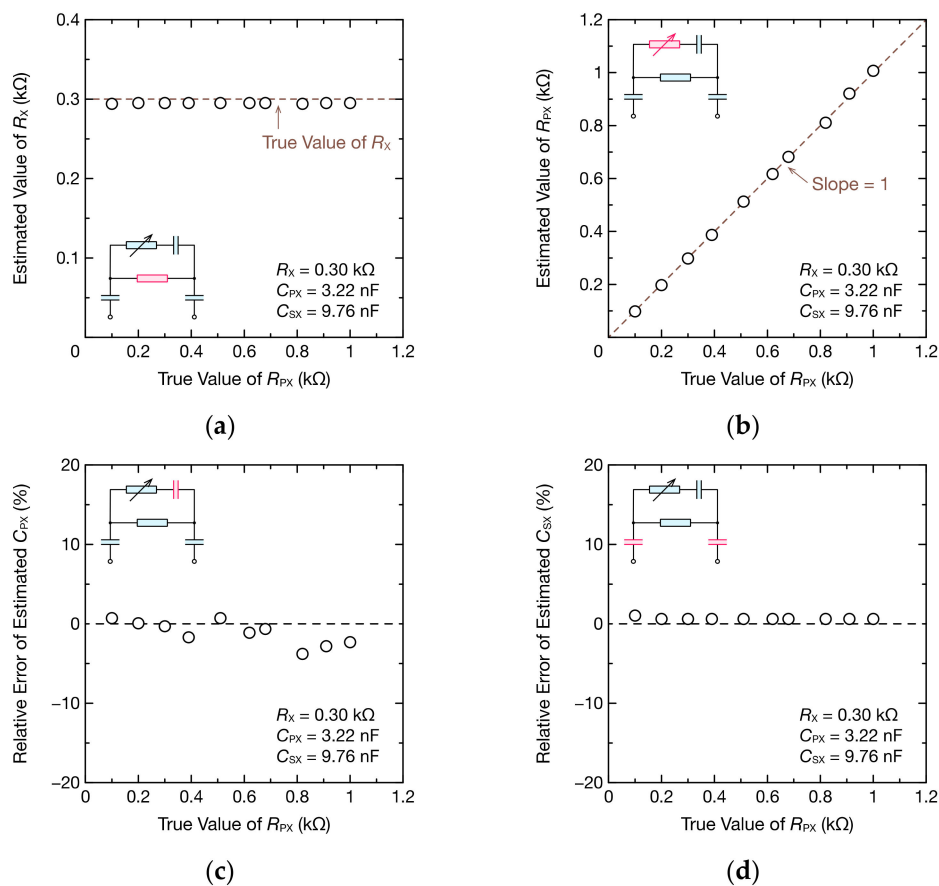


Figure 12. R_X , C_{PX} , and C_{SX} of the bioimpedance models estimated using oscillation waveforms and DFT: (a) the estimated R_X , (b) the estimated R_{PX} , (c) relative error of the estimated C_{PX} , and (d) relative error of the estimated C_{SX} . The insets are the circuit models used for fitting, and the estimated parameters are highlighted in pink.

Figure 13 illustrates the Cole–Cole plots of the bioimpedance models excluding capacitive coupling. The Cole–Cole plot of \dot{Z}_{X1} showed semicircles expected from Equations (9) and (10), and the radius of the semicircle decreased with resistance R_{PX} .

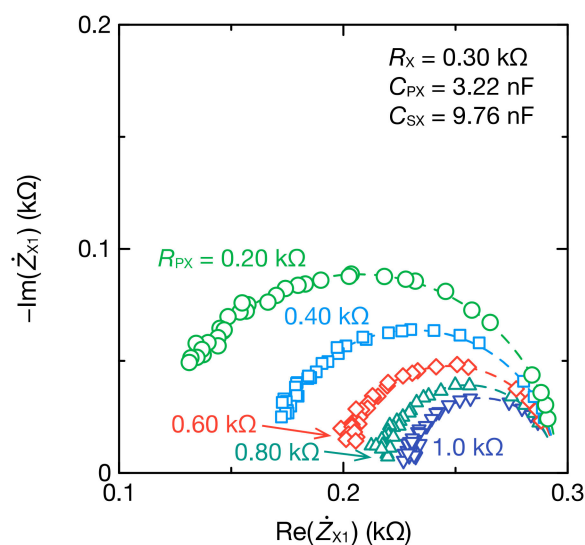


Figure 13. Cole–Cole plot of \dot{Z}_{X1} for the bioimpedance models with $C_{PX} = 3.22$ nF and $C_{SX} = 9.76$ nF. The dashed lines represent the fitting curves obtained from Equations (9) and (10).

These results demonstrate that the circuit parameters can be estimated using the proposed method, even for complex equivalent circuit models such as bioimpedance. In this study, R_F over 1 k Ω was not estimated because we designed the mode-switching oscillator to apply to biological tissue. Our proposed oscillator generates a stable oscillation waveform if the feedback resistance is sufficiently larger than the magnitudes of \dot{Z}_X and \dot{Z}_A . Therefore, the range of load that our circuit can carry depends on the feedback resistance. Resistance of less than several k Ω can be estimated when the feedback resistance is about 10 k Ω . If the feedback resistance is higher, we will be able to estimate higher resistance of about 10 k Ω .

3.2. Application of CIS to Biological Tissues

An example of the application of impedance measurement in the biomedical field is the monitoring of cauterization in catheter ablation. We, therefore, used CIS to measure the local change in impedance when porcine myocardium was coagulated. Stable oscillations with four modes of oscillating frequencies were obtained when the electrodes in Figure 2b and the surface of the porcine myocardium were in contact. Figure 14 shows the spectrum of the real part of the impedance \dot{Z}_X calculated using DFT from the obtained waveform. The equivalent circuit of biological tissues, such as porcine myocardium, is approximated using a bioimpedance model. Therefore, the real part of the impedance decreased with increasing frequency as the capacitance of cell membranes decreases. Moreover, because the measurement area included regions other than the ablation site, the impedance was larger than the local impedance (approximately 0.10 k Ω) measured through a commercial catheter ablation system. When electrocautery was performed, the impedance of the porcine myocardium decreased, regardless of the frequency range. Because cell membranes at the ablation site have high ion permeability, this decrease in impedance indicates that a part of the myocardium was degenerated through coagulation. The DFT data partially agree with the fitting curve produced by Equation (9), but the DFT data tended to be larger than the fitted data in low-frequency ranges. Furthermore, when C_{SX} was estimated using Equation (10) from the DFT data of the imaginary part of the impedance, the value before ablation was 7.98 nF and the value after ablation was 8.29 nF, both of which are low values compared to the capacitance of the PP film capacitor used, which was 9.76 nF. This suggests that resistance and capacitance components also exist between the surface of the porcine myocardium and electrodes. Therefore, to estimate circuit parameters with high accuracy, applying an equivalent circuit model is necessary considering the impedance of the interface of the myocardium and electrodes.

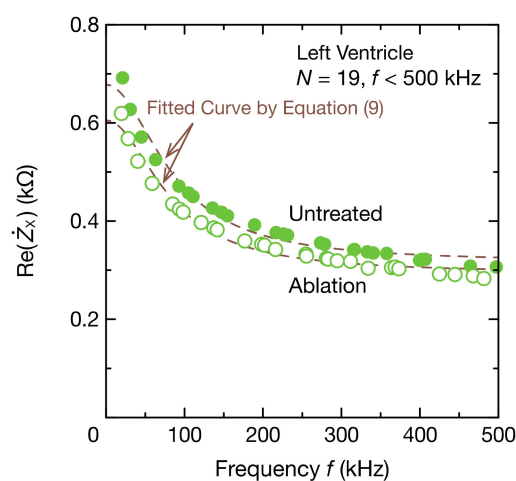


Figure 14. Frequency spectrum of the real part $\text{Re}(\dot{Z}_X)$ of the impedance \dot{Z}_X of the porcine myocardium and coupling capacitance. DFT data were fitted to Equation (9) to determine R_X , R_{PX} , and C_{PX} (dashed lines).

Figure 15 shows the frequency spectra of the porcine myocardium. \dot{Z}_{X1} in Figure 15 represents the impedance of the porcine myocardium only, excluding the impedance of the capacitive coupling C_{SX} from \dot{Z}_X . Here, C_{SX} uses a value estimated through fitting, not the capacitance value of the PP film capacitor. The Cole–Cole plot of the porcine myocardium formed a semicircle, as expected from the bioimpedance model, but the semicircle was distorted (Figure 15a). This may be because the impedance between the surface of the porcine myocardium and electrodes was not considered or because the impedance of the myocardial tissue was not uniform. When the myocardium was ablated, the magnitude of the imaginary part of the impedance also decreased, similar to the real part (Figure 15b,c), as did the radius of the semicircle in the Cole–Cole plot.

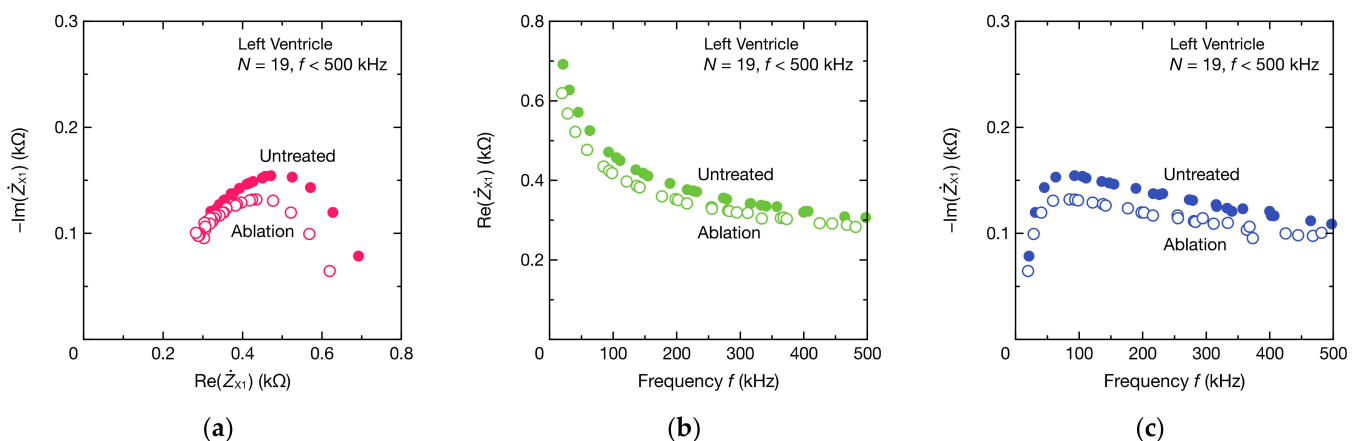


Figure 15. Frequency spectra of the impedance \dot{Z}_{X1} of the porcine myocardium: (a) the Cole–Cole plot, (b) the real part $\text{Re}(\dot{Z}_{X1})$, and (c) the imaginary part $\text{Im}(\dot{Z}_{X1})$. \dot{Z}_{X1} represents the impedance obtained by subtracting the impedance of the estimated C_{SX} from \dot{Z}_X . $\text{Re}(\dot{Z}_{X1})$ equals $\text{Re}(\dot{Z}_X)$ in Figure 14.

Furthermore, impedance was measured at four locations using CIS for each of the three porcine myocardium samples. Figure 16 shows the result of estimating R_X , R_{PX} , and C_{PX} from the determined impedance spectra. Ablation decreased the resistive components R_X and R_{PX} and increased the capacitive component C_{PX} in all 12 samples. A paired t-test on the obtained samples also showed significant differences at a significance level of 0.1%, indicating that CIS can measure changes in impedance associated with myocardial tissue degeneration.

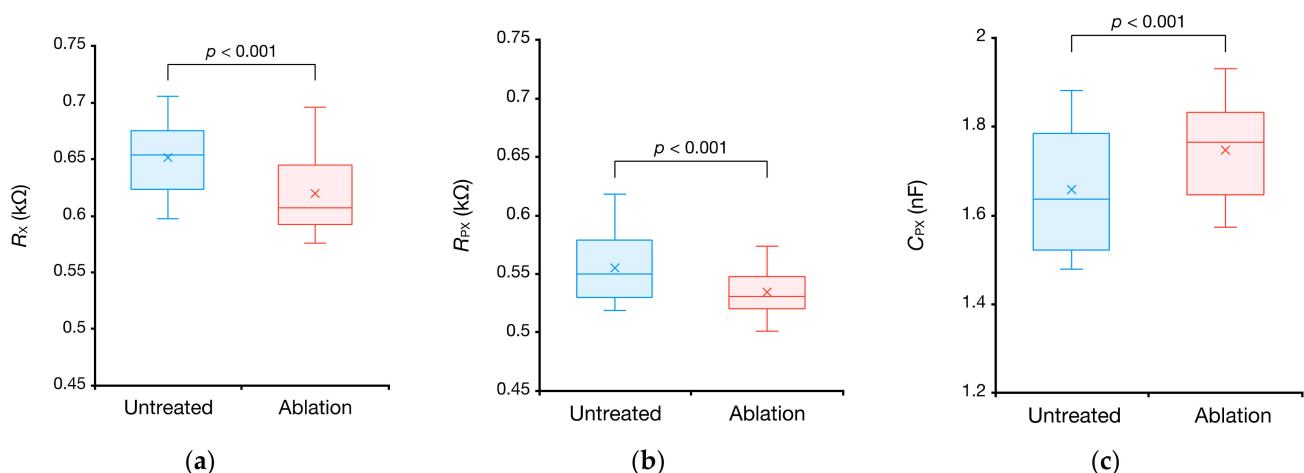


Figure 16. Comparison of equivalent circuit parameters between the untreated and ablated left ventricles of porcine hearts: (a) R_X , (b) R_{PX} , and (c) C_{PX} . The sample size is 12.

3.3. Continuous Impedance Measurement Using CIS

Figure 17 shows the oscillation waveform when a CdS photocoupler and a 9.76 nF PP film capacitor are connected in series as Z_X (Figure 3a). Measurement was started with a current I_{Ph} of 0.6 mA flowing through the LED, and the current I_{Ph} was increased instantaneously to 2.0 mA at 10 ms after the start of the measurement. Thereafter, the current I_{Ph} was returned to 0.6 mA again at 23 ms after the start of the measurement. Figure 17a shows that the switching of the current I_{Ph} changed the peak-to-peak value of the voltage $v_1(t)$, indicating that the resistance of the CdS cell changed. The peak-to-peak value V_{PP} of the voltage $v_1(t)$ is expressed by the following equation:

$$V_{PP} = \frac{R_A}{R_F}(V_P - V_N) + \frac{R_A}{R_F} \left[\frac{2R_F}{R_A + R_X + R_F} - 1 \right] (V_H - V_L). \quad (11)$$

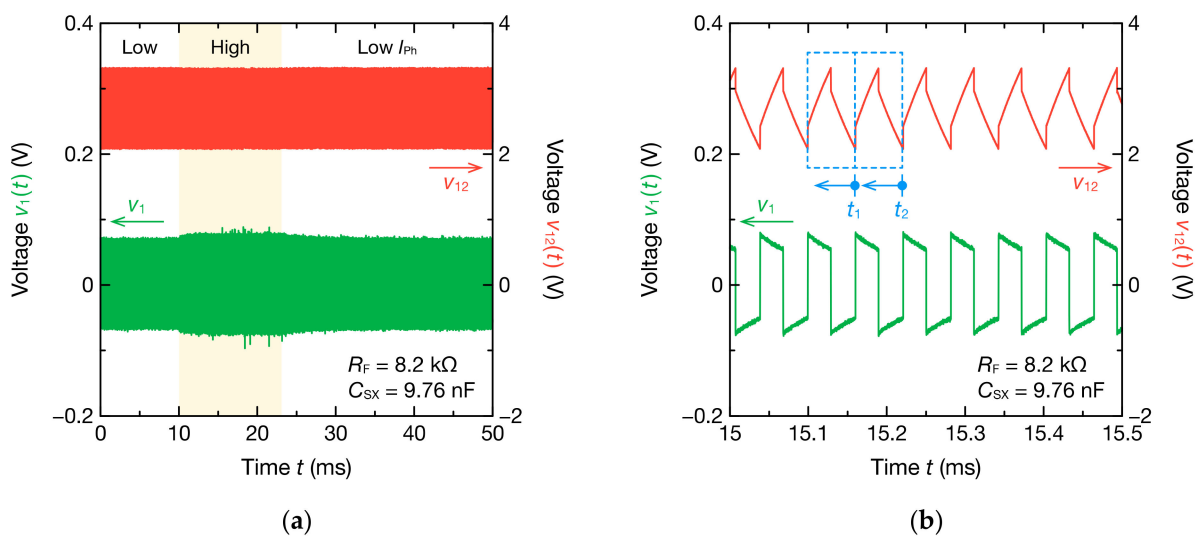


Figure 17. Single-mode oscillation waveforms of $v_{12}(t)$ and $v_1(t)$ for the nonsinusoidal oscillator incorporating the CdS photocell (Figure 3a): (a) full waveform and (b) enlarged waveform. The photocurrent I_{Ph} of the photocoupler is changed at 10 and 23 ms. The high and low levels of I_{Ph} are 2.0 and 0.6 mA, respectively. Circuit parameters are estimated for each cycle (blue dashed line). Representative points of time in each cycle are the ends of the cycles such as t_1 and t_2 .

As shown in this equation, V_{PP} increases with decreasing resistance R_X . Figure 17b indicates that a stable oscillation was obtained.

Continuous frequency spectra were obtained through DFT from the waveforms of the respective cycles of Figure 17a, and the resistance R_X of the CdS photocell could be estimated by applying Equation (7). The temporal waveform of R_X obtained by estimation is presented in Figure 18a. When I_{Ph} was increased instantaneously, R_X gradually decreased and then saturated at approximately 10 ms after the current increased. Because the response time of the CdS photocell used is relatively short, approximately 2.5 ms, this change in R_X reflects the optical response of the CdS photocell. The increase from 24 ms indicates that the resistance of the photocell increased with the reduction in I_{Ph} . Generally, the recovery time of the photocell is slower than the response time. Therefore, the gradual increase in the resistance is a reasonable response. Figure 18b compares the saturated and true values of R_X at various I_{Ph} values. The error between the estimated and true R_X values was 29 Ω at the maximum, and thus R_X could be estimated accurately.

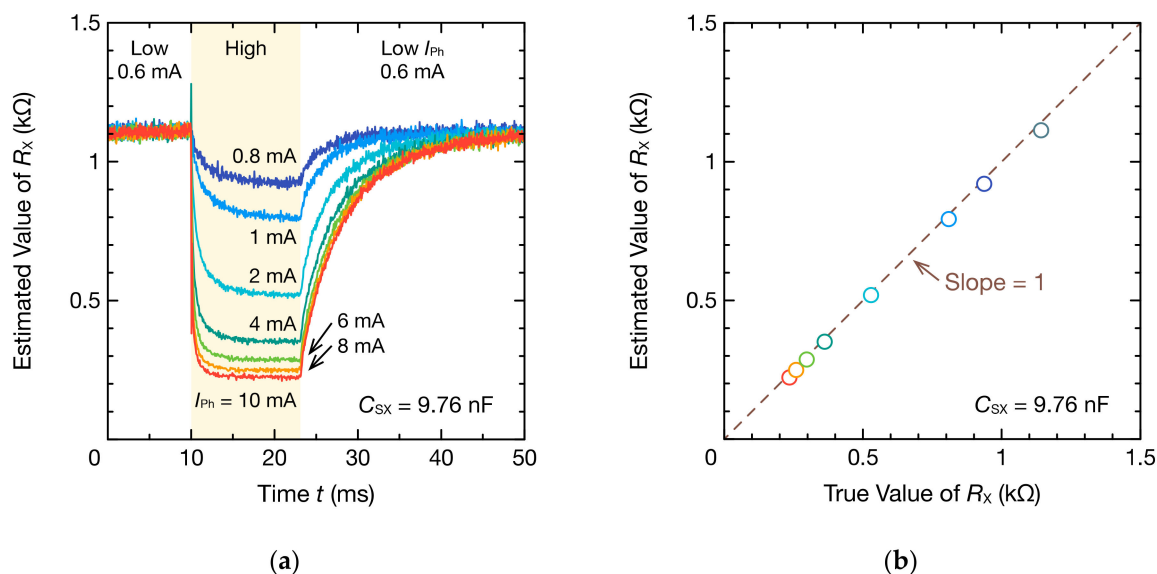


Figure 18. Resistance R_X of the photocell estimated using oscillation waveforms in Figure 17a and DFT: (a) time–resistance curves and (b) saturation values at a high I_{Ph} period. Time of the time–resistance curves corresponds to the representative points of time in Figure 17b.

Moreover, a CdS photocell was incorporated as R_X or R_{PX} in the bioimpedance model (Figure 3b,c), and the resistance of the CdS photocell was changed over time. Figure 19 shows the oscillation waveform when the resistance of the CdS photocell was changed temporally as R_X . Measurement began with a current I_{Ph} of 4.0 mA flowing through the LED, and the current I_{Ph} was increased instantaneously to 8.0 mA at 10 ms after the measurement began. Thereafter, I_{Ph} was returned to 4.0 mA again at 23 ms after the start of the measurement. R_F was 3.3 or 5.1 kΩ, and mode switching was performed in two modes.

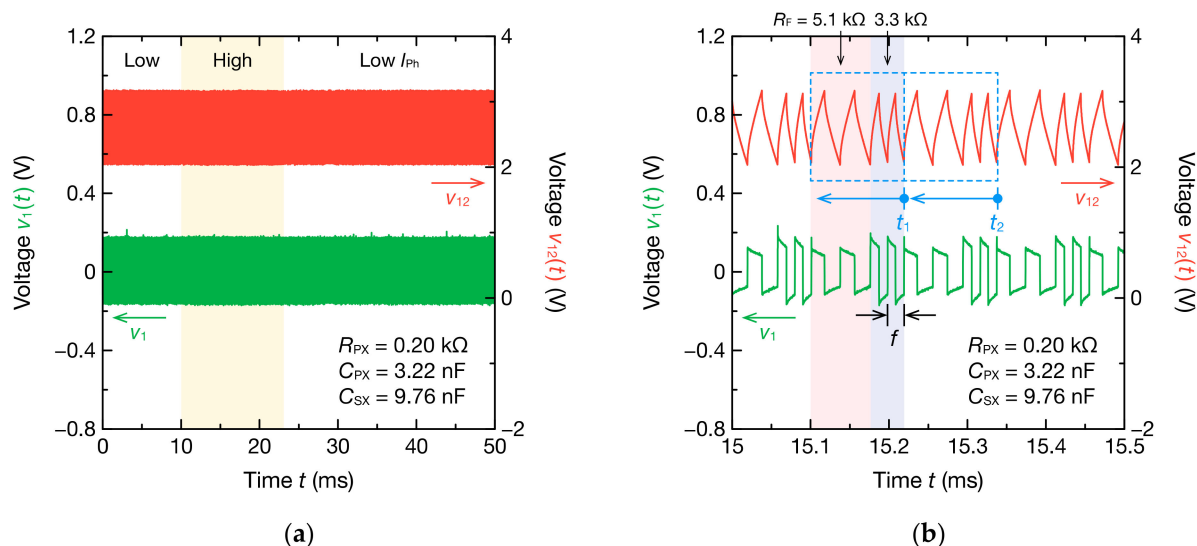


Figure 19. Two-mode oscillation waveforms of $v_{12}(t)$ and $v_1(t)$ for the nonsinusoidal oscillator incorporating the CdS photocell and circuit elements of the bioimpedance model (Figure 3b): (a) full waveform and (b) enlarged waveform. The photocurrent I_{Ph} of the photocoupler is changed at 10 and 23 ms. The high and low levels of I_{Ph} are 8.0 and 4.0 mA, respectively. Circuit parameters are estimated for each cycle (blue dashed line). Representative points of time in each cycle are the ends of the cycles such as t_1 and t_2 . The frequency f is the oscillation frequency obtained from the second half cycle of the oscillation waveform at $R_F = 3.3$ kΩ.

A stable oscillation was obtained, as illustrated in Figure 19b, and the oscillation frequency switched in two modes. A V_{PP} change was not observed because the change in I_{Ph} was smaller than that shown in Figure 17a. Although Equation (11) is not strictly valid when C_{PX} is included in \dot{Z}_X , V_{PP} depends on R_X connected in parallel with R_{PX} and C_{PX} . However, because the resistance change due to the switching of I_{Ph} was only about $0.1\text{ k}\Omega$, the V_{PP} change was negligibly small. Further, when the temporal change in R_X , R_{PX} , and C_{PX} was estimated through the DFT analysis of the oscillation waveform, only R_X changed according to the change in the CdS photocell resistance (Figure 20a). Furthermore, even when R_{PX} and C_{PX} are connected in parallel with R_X , the oscillation frequency changes with R_X of the measured object and is not significantly affected by electrical noise. Therefore, when the equivalent circuit model of the measured object is unknown or the signal-to-noise ratio in the circuit is low, the oscillation frequency can be used for monitoring the circuit parameters. However, the change in R_{PX} was not reflected in the oscillation frequency when the CdS photocell was incorporated as R_{PX} (Figure 20b). The oscillation frequency also depends on the impedance \dot{Z}_X including R_{PX} . However, R_{PX} is connected in series with C_{PX} , and C_{PX} has a relatively large impedance at the oscillation frequency. Therefore, the change in R_{PX} does not significantly contribute to the changes in \dot{Z}_X , which leads to no change in the oscillation frequency.

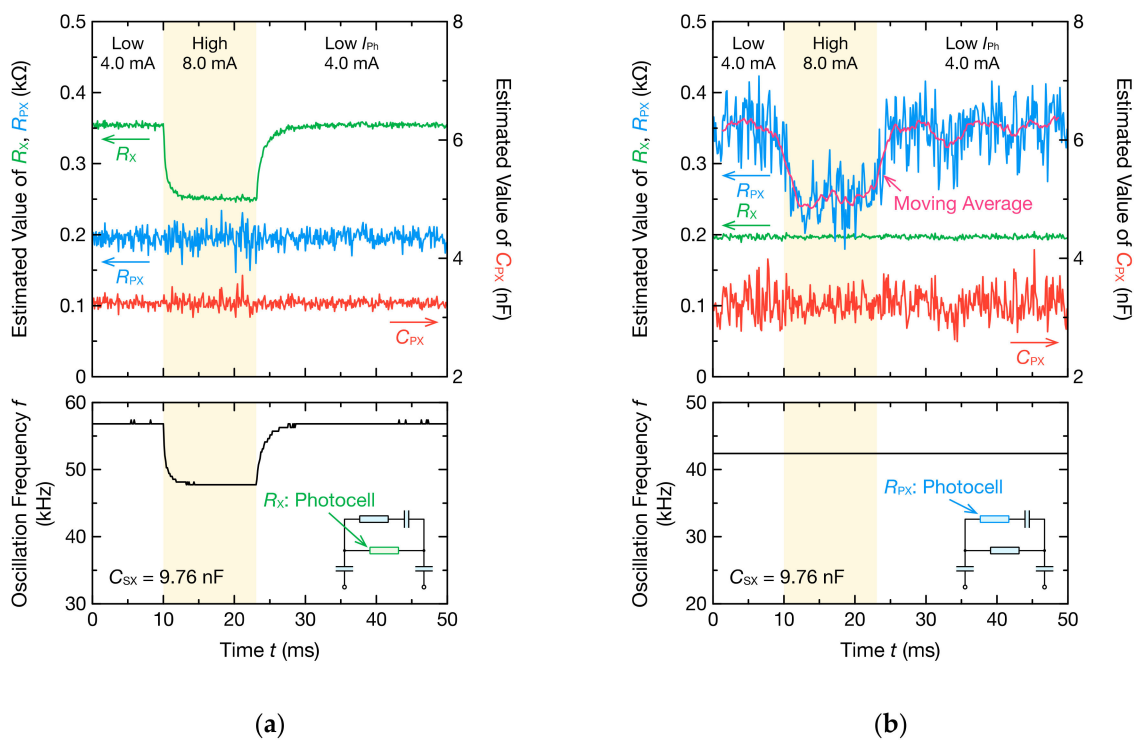


Figure 20. Time–resistance, time–capacitance, and time–frequency curves of the resistance of the photocell and circuit elements of the bioimpedance model estimated using oscillation waveforms and DFT. The photocell was used as (a) R_X or (b) R_{PX} . The other resistance is $0.20\text{ k}\Omega$; the capacitance C_{PX} is 3.22 nF ; and the capacitance C_{SX} is 9.76 nF . The times of these curves correspond to the representative points of time in Figure 19b. The insets are photocell-incorporated circuits.

DFT analysis indicated that only R_{PX} changed, but the dispersion of the data was particularly large for R_{PX} . The estimation accuracy of R_{PX} depends on the measurement accuracy of the impedance in high-frequency ranges, but the spectra of high-frequency ranges are susceptible to noise because the signal of the harmonic component is smaller than the fundamental frequency component. Therefore, the estimation accuracy of R_{PX} may be poor. However, because one segment of the oscillation waveform is sufficiently short and the time resolution is high, the estimation accuracy can be improved by considering

the moving average. The above results indicate that the proposed method can be used to continuously monitor the temporal variation in impedance.

4. Conclusions

We fabricated a mode-switching nonsinusoidal oscillator to accurately estimate the circuit parameters of impedance, including multiple resistances and capacitances, using CIS. The oscillation waveform of the fabricated circuit had multiple oscillation frequencies caused by the periodic switching of the feedback resistor. This enabled us to obtain a broader frequency spectrum range with a higher resolution than a single oscillation frequency through DFT analysis. Further, the circuit parameters of complicated circuit models such as RC parallel circuits and bioimpedance models could also be estimated accurately from the oscillation waveforms of this circuit.

We applied CIS using the mode-switching nonsinusoidal oscillator to impedance measurement of porcine myocardium. Consequently, the changes in the local impedance spectrum caused by the coagulation of the porcine myocardium could be measured. Moreover, the resistive components decreased and the capacitive components increased during electrocautery by fitting the impedance spectra with the bioimpedance model. By measuring and analyzing the continuous oscillation waveform when a CdS photocell was incorporated into the mode-switching nonsinusoidal oscillator, measuring the changes in impedance over time was possible.

These findings demonstrate that temporal changes in the impedance of biological tissues can be monitored using our proposed method. However, because this study excluded the impedance measurements of biological tissues through capacitive coupling using an insulator, future studies should aim to apply CIS to biological tissues covered with an insulator, such as the human body with clothing.

Author Contributions: Conceptualization, A.U.; methodology, A.U.; software, T.Y.; validation, T.Y.; formal analysis, T.Y.; investigation, T.Y., E.O., and A.U.; resources, E.O. and A.U.; data curation, T.Y.; writing—original draft preparation, T.Y. and A.U.; writing—review and editing, T.Y., E.O., and A.U.; visualization, T.Y.; supervision, A.U.; project administration, A.U.; funding acquisition, A.U. All authors have read and agreed to the published version of the manuscript.

Funding: This research was supported, in part, by the SECOM Science and Technology Foundation and, in part, by the Private University Research Branding Project supported by MEXT, Japan.

Institutional Review Board Statement: Not applicable.

Informed Consent Statement: Not applicable.

Data Availability Statement: The data that support the findings of this study are available from the corresponding author, A.U., upon reasonable request.

Conflicts of Interest: The authors declare no conflict of interest.

References

1. Grossi, M.; Riccò, B. Electrical impedance spectroscopy (EIS) for biological analysis and food characterization: A review. *J. Sens. Sens. Syst.* **2017**, *6*, 303–325. [[CrossRef](#)]
2. Szuster, B.; Roj, Z.S.D.; Kowalski, P.; Sobotnicki, A.; Woloszyn, J. Idea and measurement methods used in bioimpedance spectroscopy. *Adv. Intell. Syst. Comput.* **2017**, *623*, 70–78.
3. Davies, S.J.; Davenport, A. The role of bioimpedance and biomarkers in helping to aid clinical decision-making of volume assessments in dialysis patients. *Kidney Int.* **2014**, *86*, 489–496. [[CrossRef](#)] [[PubMed](#)]
4. Piccoli, A. Bioelectric impedance measurement for fluid status assessment. *Contrib. Nephrol.* **2010**, *164*, 143–152. [[PubMed](#)]
5. Jaffrin, M.Y.; Morel, H. Body fluid volumes measurements by impedance: A review of bioimpedance spectroscopy (BIS) and bioimpedance analysis (BIA) methods. *Med. Eng. Phys.* **2008**, *30*, 1257–1269. [[CrossRef](#)] [[PubMed](#)]
6. Kyle, U.G.; Bosaeus, I.; De Lorenzo, A.D.; Deurenberg, P.; Elia, M.; Gómez, J.M.; Heitmann, B.L.; Kent-Smith, L.; Melchior, J.-C.; Pirlich, M.; et al. Bioelectrical impedance analysis—Part I: Review of principles and methods. *Clin. Nutr.* **2004**, *23*, 1226–1243. [[CrossRef](#)]

7. Kyle, U.G.; Bosaeus, I.; De Lorenzo, A.D.; Deurenberg, P.; Elia, M.; Gómez, J.M.; Heitmann, B.L.; Kent-Smith, L.; Melchior, J.-C.; Pirlich, M.; et al. Bioelectrical impedance analysis—Part II: Utilization in clinical practice. *Clin. Nutr.* **2004**, *23*, 1430–1453. [[CrossRef](#)]
8. Demura, S.; Sato, S.; Kitabayashi, T. Percentage of total body fat as estimated by three automatic bioelectrical impedance analyzers. *J. Physiol. Anthropol. Appl. Hum. Sci.* **2004**, *23*, 93–99. [[CrossRef](#)]
9. Cha, K.; Chertow, G.M.; Gonzalez, J.; Lazarus, J.M.; Wilmore, D.W. Multifrequency bioelectrical impedance estimates the distribution of body water. *J. Appl. Physiol.* **1995**, *79*, 1316–1319. [[CrossRef](#)]
10. Groenendaal, W.; Lee, S.; van Hoof, C. Wearable bioimpedance monitoring: Viewpoint for application in chronic conditions. *JMIR Biomed. Eng.* **2021**, *6*, e22911. [[CrossRef](#)]
11. Sel, K.; Osman, D.; Jafari, R. Non-invasive cardiac and respiratory activity assessment from various human body locations using bioimpedance. *IEEE Open J. Eng. Med. Biol.* **2021**, *2*, 210–217. [[CrossRef](#)] [[PubMed](#)]
12. Zink, M.D.; König, F.; Weyer, S.; Willmes, K.; Leonhardt, S.; Marx, N.; Napp, A. Segmental bioelectrical impedance spectroscopy to monitor fluid status in heart failure. *Sci. Rep.* **2020**, *10*, 3577. [[CrossRef](#)] [[PubMed](#)]
13. Collins, C.T.; Reid, J.; Makrides, M.; Lingwood, B.E.; McPhee, A.J.; Morris, S.A.; Gibson, R.A.; Ward, L.C. Prediction of body water compartments in preterm infants by bioelectrical impedance spectroscopy. *Eur. J. Clin. Nutr.* **2013**, *67*, S47–S53. [[CrossRef](#)] [[PubMed](#)]
14. Piccoli, A.; Rossi, B.; Pillon, L.; Bucciante, G. A new method for monitoring body fluid variation by bioimpedance analysis: The RXc graph. *Kidney Int.* **1994**, *46*, 534–539. [[CrossRef](#)] [[PubMed](#)]
15. Nwosu, A.C.; Mayland, C.R.; Mason, S.; Cox, T.F.; Varro, A.; Ellershaw, J. The association of hydration status with physical signs, symptoms and survival in advanced cancer—The use of bioelectrical impedance vector analysis (BIVA) technology to evaluate fluid volume in palliative care: An observational study. *PLoS ONE* **2016**, *11*, e0163114. [[CrossRef](#)]
16. Toso, S.; Piccoli, A.; Gusella, M.; Menon, D.; Crepaldi, G.; Bononi, A.; Ferrazzi, E. Bioimpedance vector pattern in cancer patients without disease versus locally advanced or disseminated disease. *Nutrition* **2003**, *19*, 510–514. [[CrossRef](#)]
17. Nescolarde, L.; Piccoli, A.; Román, A.; Núñez, A.; Morales, R.; Tamayo, J.; Doñate, T.; Rosell, J. Bioelectrical impedance vector analysis in haemodialysis patients: Relation between oedema and mortality. *Physiol. Meas.* **2004**, *25*, 1271–1280. [[CrossRef](#)]
18. Piccoli, A.; Italian CAPD-BIA Study Group. Bioelectric impedance vector distribution in peritoneal dialysis patients with different hydration status. *Kidney Int.* **2004**, *65*, 1050–1063. [[CrossRef](#)]
19. Bozzetto, S.; Piccoli, A.; Montini, G. Bioelectrical impedance vector analysis to evaluate relative hydration status. *Pediatr. Nephrol.* **2010**, *25*, 329–334. [[CrossRef](#)]
20. Da Fonseca, R.D.; Santos, P.R.; Monteiro, M.S.; Fernandes, L.A.; Campos, A.H.; Borges, D.L.; Rosa, S.S.R.F. Parametric evaluation of impedance curve in radiofrequency ablation: A quantitative description of the asymmetry and dynamic variation of impedance in bovine ex vivo model. *PLoS ONE* **2021**, *16*, e0245145. [[CrossRef](#)]
21. Barkagan, M.; Rottmann, M.; Leshem, E.; Shen, C.; Buxton, A.E.; Anter, E. Effect of baseline impedance on ablation lesion dimensions: A multimodality concept validation from physics to clinical experience. *Circ. Arrhythm. Electrophysiol.* **2018**, *11*, e006690. [[CrossRef](#)]
22. Sulkin, M.S.; Laughner, J.I.; Hilbert, S.; Kapa, S.; Kosiuk, J.; Younan, P.; Romero, I.; Shuros, A.; Hamann, J.J.; Hindricks, G.; et al. Novel measure of local impedance predicts catheter—Tissue contact and lesion formation. *Circ. Arrhythm. Electrophysiol.* **2018**, *11*, e005831. [[CrossRef](#)]
23. Chinitz, J.S.; Michaud, G.F.; Stephenson, K. Impedance-guided radiofrequency ablation: Using impedance to improve ablation outcomes. *Innov. Card. Rhythm. Manag.* **2017**, *8*, 2868–2873. [[CrossRef](#)]
24. Yamaguchi, T.; Ueno, A. Capacitive-coupling impedance spectroscopy using a non-sinusoidal oscillator and discrete-time Fourier transform: An introductory study. *Sensors* **2020**, *20*, 6392. [[CrossRef](#)]
25. Takano, M.; Ueno, A. Noncontact in-bed measurements of physiological and behavioral signals using an integrated fabric-sheet sensing scheme. *IEEE J. Biomed. Health Inform.* **2019**, *23*, 618–630. [[CrossRef](#)]
26. Elghajji, A.; Wang, X.; Weston, S.D.; Zeck, G.; Hengerer, B.; Tosh, D.; Rocha, P.R.F. Electrochemical impedance spectroscopy as a tool for monitoring cell differentiation from floor plate progenitors to midbrain neurons in real time. *Adv. Biol.* **2021**, *5*, 2100330. [[CrossRef](#)] [[PubMed](#)]
27. Sato, H.; Nakamura, T.; Kusuhara, T.; Kenichi, K.; Kuniyasu, K.; Kawashima, T.; Hanayama, K. Effectiveness of impedance parameters for muscle quality evaluation in healthy men. *J. Physiol. Sci.* **2020**, *70*, 53. [[CrossRef](#)] [[PubMed](#)]
28. Lu, F.; Wang, C.; Zhao, R.; Du, L.; Fang, Z.; Guo, X.; Zhao, Z. Review of stratum corneum impedance measurement in non-invasive penetration application. *Biosensors* **2018**, *8*, 31. [[CrossRef](#)] [[PubMed](#)]
29. Hernández-Balaguera, E.; López-Dolado, E.; Polo, J.L. Obtaining electrical equivalent circuits of biological tissues using the current interruption method, circuit theory and fractional calculus. *RSC Adv.* **2016**, *6*, 22312. [[CrossRef](#)]
30. Münkler, P.; Gunawardene, M.A.; Jungen, C.; Klatt, N.; Schwarzl, J.M.; Akbulak, R.Ö.; Dinshaw, L.; Hartmann, J.; Jularic, M.; Kahle, A.K.; et al. Local impedance guides catheter ablation in patients with ventricular tachycardia. *J. Cardiovasc. Electrophysiol.* **2020**, *31*, 61–69. [[CrossRef](#)]